frontiers | Frontiers in Earth Science

TYPE Original Research
PUBLISHED 05 September 2024
DOI 10.3389/feart.2024.1437599

OPEN ACCESS

EDITED BY
Hongjian Zhu,
Yanshan University, China

REVIEWED BY
Yan Jing,
Jilin University, China
Ali Raza,
University of Houston, United States
Sun Jinggui,
College of Earth Sciences, Jilin University, China

*CORRESPONDENCE
Peng Zhang,
geozhangpeng2010@163.com
Xiaogang Xue,
kc_xxg@ccit.edu.cn

RECEIVED 24 May 2024
ACCEPTED 22 August 2024
PUBLISHED 05 September 2024

CITATION
Xue X, Zhang P, Chen G, Zhang H and Zhang X (2024) Genesis of Permian granitoids in the southeast of Inner Mongolia and their response to the Xing'an-Mongolia orogenic belt evolution: constraints from zircon U-Pb age, geochemistry and Hf isotopes.
Front. Earth Sci. 12:1437599.
doi: 10.3389/feart.2024.1437599

Genesis of Permian granitoids in the southeast of Inner Mongolia and their response to the Xing'an-Mongolia orogenic belt evolution: constraints from zircon U-Pb age, geochemistry and Hf isotopes

Xiaogang Xue[1]*, Peng Zhang[2]*, Guoqiang Chen[1], Haihong Zhang[1] and Xuebin Zhang[3]

[1]School of Prospecting and Surveying Engineering, Changchun Institute of Technology, Changchun, China, [2]Shenyang Geological Survey Center, China Geological Survey, Shenyang, China, [3]Tianjin Geological Survey Institute, Tianjin, China

Research on the geological process of the Xing'an - Mongolia Orogenic Belt has attracted the attention of scholars both domestically and internationally. Its genesis and tectonic location may help revealing the geological processes asscoaited with the evolution of the Xing'an - Mongolia Orogenic Belt. This study focuses on the development of the Permian granitic complex in Jielin Ranch, and we conduct systematic geological, petrographic, zircon U-Pb chronology, Hf isotope, and geochemical tracing of rock elements for evidence. The results show that the granitic complex is mainly composed of monzogranite and syenogranite, which obtained zircon U-Pb ages of 291.1 ± 1.1 Ma and 260.8 ± 1.1 Ma, respectively. The monzogranite and syenogranite are all acidic and aluminum rich rocks, and the monzogranite is a potassium rich, high potassium calcium alkaline rock series with relatively low REE content, high degree of fractionation, and insignificant europium anomalies, enriched with LILE (Rb, Th, U, K), deficient elements such as Ba, Sr, Nb, Ti, and P, εHf(t) values are from +4.1 to +7.0 (T_{DM2}=1130–920 Ma). Geochemistry shows that the monzogranite belongs to high fractionation of I-type granite, which formed in a subduction-compressional or extension tectonic environment, and Middle Neoproterozoic lower crust rocks as the major source material of magma. The syenogranite is a potassium high potassium transitional rock series with a high rare earth content (214×10^{-6}~325×10^{-6}), low LREE/HREE (2.54–6.41), δEu (0.04–0.15) and the typical "four component effect" fractionation mode is enriched in large ion lithophilic elements such as Rb, Th, K, and strongly depleted in elements such as Ba, Sr, Nb, Ta, Ti, P, εHf(t) values are from +4.2 to +8.6 (T_{DM2}=738–1228 Ma), suggesting the characteristics of an "A_2 type" granite. The magma originated from partial melting of the lower crust of the Middle and Neoproterozoic with the participation of mantle derived melts, and was formed in a back-arc extensional environment. This suggests that the study area experienced a subduction-compressional or extension tectonic

environment during the early Permian and a brief backarc extension process in the late Permian.

KEYWORDS

Jielin Ranch in eastern Inner Mongolia, Permian granitic complex, zircon U-Pb dating, Hf isotopes, petrogenesis, the Xing'an-Mongolia orogenic process

1 Introduction

The Xing'an-Mongolia orogenic belt belongs to the eastern segment of the Central Asian orogenic belt. The evolutionary process of this region has long been widely studied by scholars both domestically and internationally (Şengör et al., 1993; Xiao et al., 2015; Xiao et al., 2018; Zhang et al., 2024). Granite serves as a crucial carrier in the evolutionary process of the Xing'an-Mongolia orogenic belt, and research on its formation age and rock genesis can effectively constrain the orogenic process. The study area is located in the central part of the Xing'an-Mongolia orogenic belt, representing a region of Late Paleozoic tectonic activity within the orogenic belt. It has preserved crucial geological evidence of microcontinents, trench-arc basin systems, and ocean-land transformations during the continuous southward and northward subduction and eventual closure of the ancient Asian ocean. Consequently, it has continuously drawn attention from experts and scholars (Mao et al., 2013; Kröner et al., 2014; Wilde, 2015; Xiao et al., 2015; 2018). However, there are still numerous controversies regarding the evolutionary processes, structural patterns, and mineralization mechanisms of the Xing'an-Mongolia orogenic belt. The unresolved scientific issues include 1) the timing and location of the closure of the multiple ophiolite belts with respect to the final closure of the ancient Asian ocean (Song et al., 2015); 2) the coupling relationship between the Late Paleozoic large-scale deep-seated magmatic activity and the Xing'an-Mongolia orogenic process, and the existence of large-scale porphyry-type copper deposits (Zhu et al., 2022). 3) As the tectonic evolution of Xing'an-Mongolia orogenic belt is closely related to micro-continental blocks, massifs, terranes, sea mountains, and volcanic arcs in the Paleo-Asian Ocean (Kröner et al., 2007; Liu et al., 2017), the basement nature of tectonic units within eastern Paleo-Asian Ocean and the tectonic history of ocean basins between them are controversially, which seriously hinder the understanding of the tectonic evolution ofthe Xing'an-Mongolia orogenic belt (Ma et al., 2022). Therefore, this study focuses on the Late Paleozoic granitic rocks in the Jielin Ranch area northeast of Xilinhot City, Inner Mongolia, in the central part of the Xing'an-Mongolia orogenic belt. In this study, we conducted systematic geological surveys, lithofacies observations, LA-ICP-MS zircon U-Pb dating, rock elemental and zircon Hf isotope analyses. Based on the discussions of the Late Paleozoic granitic rocks genesis, this study discusses the relationship between magmatic activity and geodynamic background and provides evidence for further understanding the evolution of the Xing'an-Mongolia orogenic process. This study provides new information to help better understand the porphyry-type copper mineralization and regional metallogeny in the Xing'an - Mongolia orogenic belt.

2 Regional geology and geological overview of the study area

The study area is located in the northeastern part of Xilinhot City, and situated in the central portion of the Xilinhot micro-block within the eastern segment of the Xing'an-Mongolia Orogenic Belt. It is sandwiched between the Paleozoic Hegenshan ophiolitic mélange arc accretionary complex and the Late Paleozoic Solonker suture zone (Figure 1A). Presently, regional geological investigations reveal a structural pattern in this area, including the north part of the Late Paleozoic Solonker suture zone, the Late Paleozoic Solonker suture zone itself, and the southern block of the Solonker suture zone (Xiao et al., 2015). The northern block is juxtaposed with the South Mongolia composite terrane, while the southern block is contiguous with the North China Craton (Xu et al., 2018; Xiao et al., 2018) (Figure 1B). Specifically, the northern block can be divided into the Paleozoic Uriastai continental margin (Wu et al., 2011; Xu et al., 2013; Eizenhöfer et al., 2015; Xiao et al., 2015; Liu et al., 2017), the Paleozoic Hegenshan ophiolitic accretionary complex (Li et al., 2020), and the Paleozoic Xilinhot micro-block/northern orogenic belt (Xiao et al., 2015; Sun et al., 2020) (Figure 1B). The southern block is often referred to the southern orogenic belt or the Paleozoic-Early Triassic Bainaimiao arc, and it is connected to the North China Craton to the south by the Chifeng-BaiyunEbo fault (Xiao et al., 2018) (Figure 1B).

The overall structural pattern of the study area extends in a northeast direction, with a central region characterized by medium to deep-seated granitic complex, flanked by stratigraphic formations of different ages on both sides (Figure 1C). The formations exposed on the northern and southern sides mainly consist of Late Paleozoic to Mesozoic strata, with Late Paleozoic formations including the Upper Carboniferous Benbatu Formation (C_2bb), ChaganNur volcanic rocks (cv), Amushan Formation (C_2a), and Permian Lower Shoushangou Formation (P_1ŝŝ), Lower Middle Cambrian Dashizhai Formation ($P_{1\text{-}2}$dŜ), and Zhesi Formation (P_2zs). Late Mesozoic formations comprise extensively distributed Cretaceous strata, including the Baiyingaolao Formation (K_1b), Meletu Formation (K_1m), and Damoguaihe Formation (K_1d) (Figure 1C). The main intrusive body in the central region is Permian granitic rocks, with an area exceeding 10 square kilometers, characterized by granites and alkali feldspar granites (Liu J. F. et al., 2022). To the northeast and southwest are gabbros and gabbro diorites, respectively (Figure 1C). Preliminary geochronological studies suggest that the gabbros and gabbro diorites to the northeast and southwest were formed during the Carboniferous period, while the main intrusive body of Permian granitic rocks in the central region was formed during the Permian period (Zhang et al., 2011).

Mapping results indicate that the granitic complex primarily consists of medium-grained monzogranite intrusion (exposed

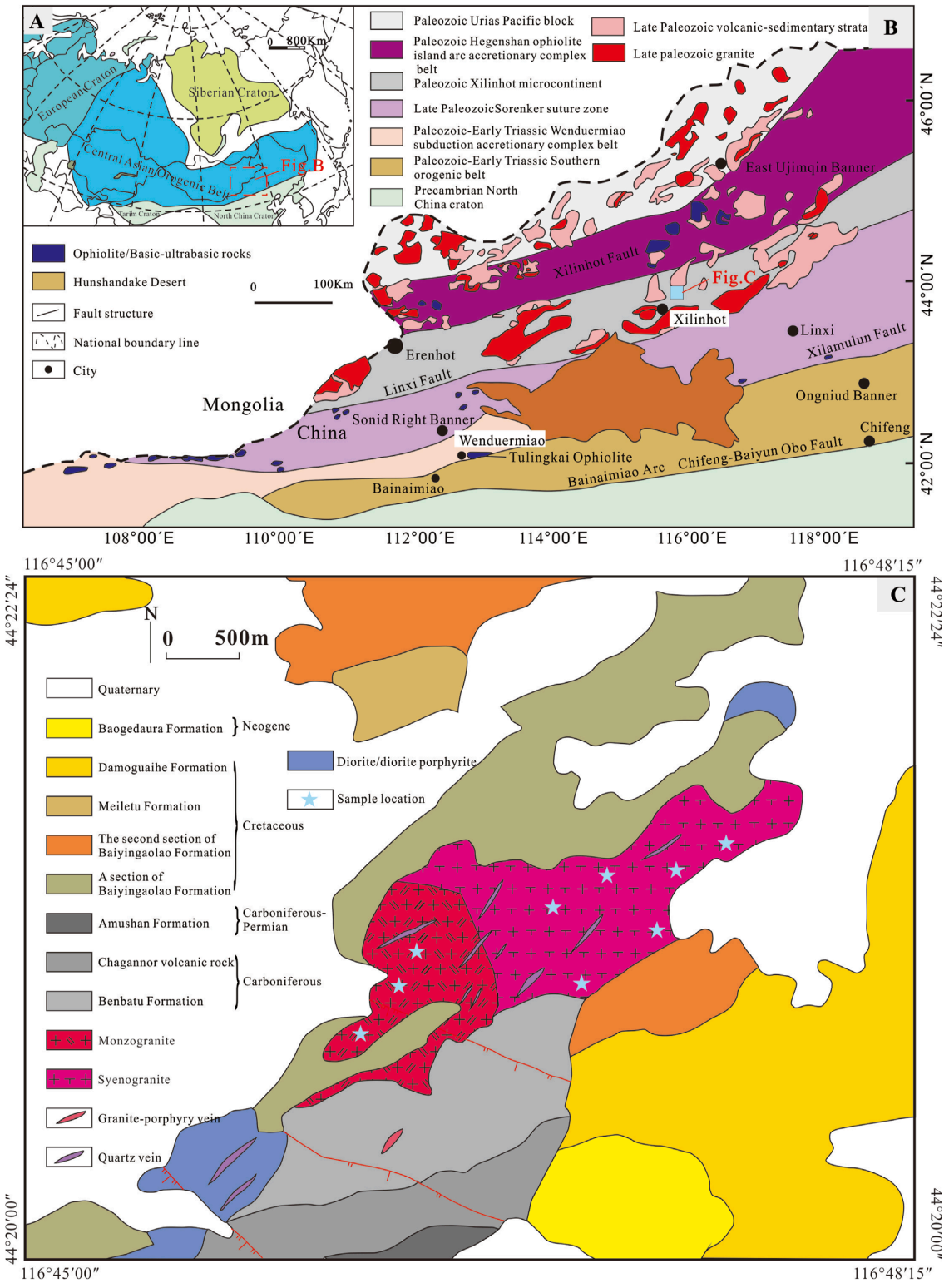

FIGURE 1
(A) Schematic diagram of the location of the Central Asian orogenic belt (modified from Jahn et al., 2000); **(B)** Map of tectonic units and distribution of igneous rocks in the southeastern part of the Central Asian orogenic belt (modified from Liu et al., 2018; Xiao et al., 2015); **(C)** Geological map and sampling location map of the southwestern part of the Jelin Ranch area (Tianjin Institute of Geological Survey, 2014).

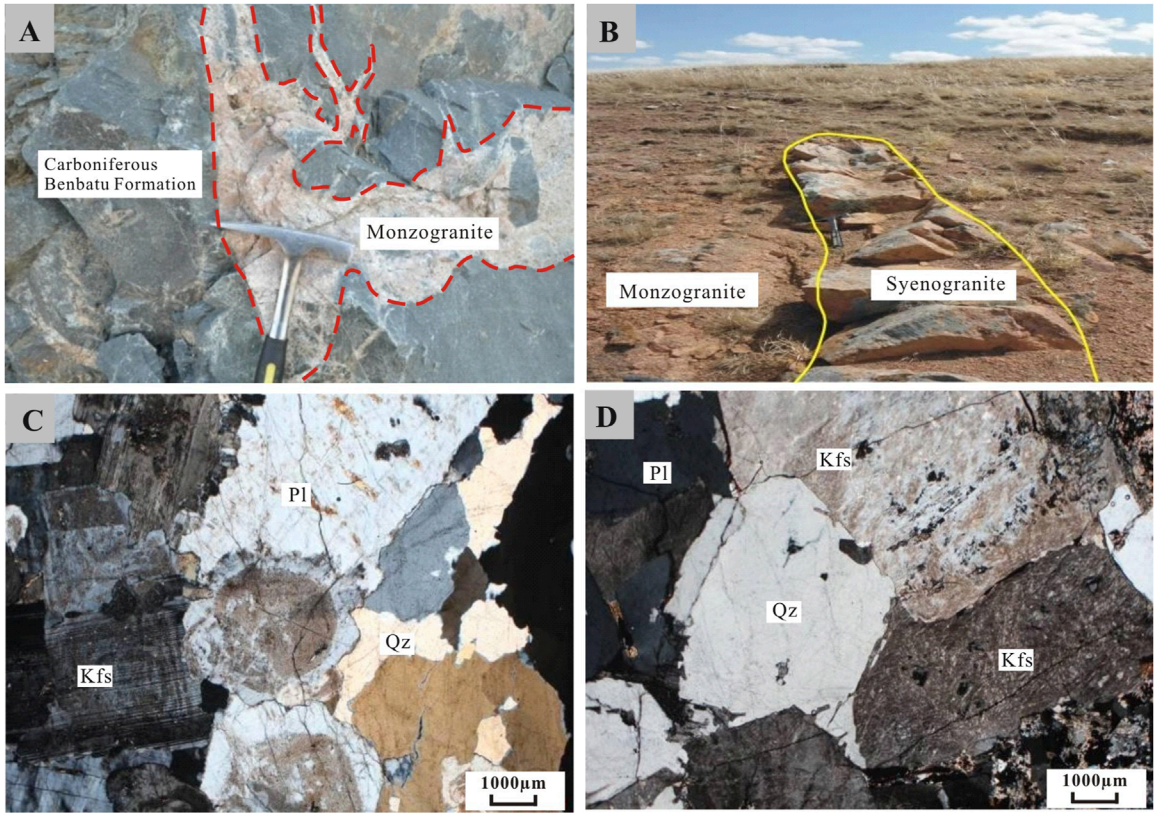

FIGURE 2
(A) Monzogranite intrudes into the Huniferous Benbatu Formation in a vein like manner; **(B)** The syenogranite intrudes into the monzogranite rock mass in a vein like manner; **(C)** Microscopic photos of diorite (orthogonally polarized, medium to coarse grained granite structure); **(D)** Photos of orthorhombic granite under a microscope (orthogonally polarized, with medium grain granite structure); Mineral abbreviations: Pl-plagioclase, Kfs-orthoclase, Qz-quartz.

area ≥2 km^2) and medium-grained syenogranite intrusion (area ≥4 km^2), with internal occurrences of granite porphyry and quartz veins (Tianjin Institute of Geological Survey, 2014). The medium-grained monzogranite intrusion is located in the southwestern part of the complex, while the syenogranite intrusion is situated in its northeastern part. The main rock phases intrude the Carboniferous Benbatu Formation strata (Figure 2A), with the syenogranite forming later than the monzogranite (Figure 2B). The relative intrusive sequence from early to late is observed as follows: medium-grained monzogranite→medium-grained syenogranite→granite porphyry and quartz veins (Figures 2A, B) (Tianjin Institute of Geological Survey, 2014).

3 Experimental samples and testing methods

The experimental samples were collected from the monzogranite and syenograniteas indicated in Figure 1C. Systematic testing of representative rock samples was conducted, including lithofacies analysis, zircon U-Pb dating, elemental analysis, and Hf isotope geochemistry.

3.1 Sample petrographic description

3.1.1 Monzogranite

The experimental sample is from the monzogranite rock phase (Figure 2A). The weathered surface of the rock appears light grayish-white, while the fresh surface exhibits a light pinkish-red color. It possesses a medium-grained granitic structure with blocky textures (Figure 2C). The main minerals consist of plagioclase feldspar (approximately 40%), potassium feldspar (approximately 35%), quartz (approximately 20%). The accessory minerals include opaque minerals (less than 1%), apatite, zircon, and magnetite. Specifically: Plagioclase feldspar is subhedral to tabular, with a grain size generally ranging from 2 to 5 mm, and exhibits sericitization. Worm-like structures associated with contact alteration with potassium feldspar are observed, indicating a more calcic composition (An = 28). Potassium feldspar occurs as subhedral to tabular grains, with well-developed twin crystals. Microcline predominates, with a grain size of 2–5 mm. It contains inclusions of plagioclase feldspar, biotite, and other minerals. Quartz occurs as subhedral to tabular grains, distributed in interstitial spaces between feldspar grains. Internal undulatory extinction is evident, indicating slight recrystallization. Biotite appears as scattered flakes, often replaced by chlorite and sericite, exhibiting pseudomorphic textures.

3.1.2 Syenogranite

This rock phase is distributed on the northeastern side of the granitic rock mass, overlain by the Baiyingaolao Formation of the Late Cretaceous. It forms an irregular "tongue-shaped" intrusive body on the inner eastern side of the complex rock mass (Figure 1B). Branch-like intrusions are visible at the edges, intruding into the Late Carboniferous Benbatu Formation strata and the Middle Permian monzogranite intrusion (Figure 2B). The weathered surface of the rock appears light pinkish-red, while the fresh surface is reddish-pink, with numerous vein networks and occurrences of opaque mineral fillings (Figure 2D). The main rock structure is medium-grained granitic, displaying blocky textures. The primary minerals consist of plagioclase feldspar (approximately 20%), potassium feldspar (approximately 45%), quartz (approximately 30%), with accessory minerals comprising about 3% of varying-sized (d=0.1–0.6 mm) opaque minerals, apatite, and zircon. Specifically: Plagioclase feldspar occurs as subhedral to tabular grains, with a grain size generally ranging from 2 to 4.5 mm, occasionally from 0.2 to 2 mm. It exhibits alteration to kaolinite and sericite, with well-developed perthitic twinning, predominantly indicating oligoclase composition (An = 40±). Potassium feldspar appears as subhedral to tabular grains, mainly microcline, with a grain size ranging from 2 to 5 mm. Quartz occurs as subhedral grains, distributed in interstitial spaces between feldspar grains, with a grain size generally ranging from 2 to 5 mm. Pronounced undulatory extinction is observed. Biotite occurs as scattered flakes, often replaced by muscovite and opaque minerals, exhibiting pseudomorphic textures.

3.2 Experimental methods

3.2.1 Zircon separation and zircon U-Pb dating, Hf isotope analysis

Zircon separation was conducted at the Hebei Institute of Regional Geology and Mineral Exploration using conventional heavy liquid and magnetic separation methods to extract zircon grains. The selected zircon samples were then manually picked under a binocular microscope, embedded in epoxy resin, and polished for cathodoluminescence (CL) studies. After CL selection, zircon U-Pb dating was carried out using the LA - ICP-MS system (Figure 3A), with experiments conducted at Beijing Gaonianlinghang Technology Co., Ltd. The laser ablation system (GeoLas 2005) utilized an ArF193 nm ultraviolet excimer laser with a spot size of 30 μm and a maximum repetition rate of 10 Hz, achieving an energy density of 13–14J/cm2. The inductively coupled plasma mass spectrometer (ICP-MS) used was the Agilent 7500a. Helium gas was employed as the carrier gas, and NIST612 was used as an external standard for the calculation of Th, U, and Pb contents. Sample standard glasses NIST 610, standard zircons 91500 and GJ-1 were used to correct for isotope fractionation during dating and to monitor analytical precision. Specific experimental procedures and detailed instrument operations can be found in the reference Hu et al., 2015. Data processing for this study was performed using the ICPMSDataCal 9.0 program.

In addition to the *in-situ* zircon U-Pb dating, zircon Hf isotope analysis was conducted for the age measurement points. The experiments were carried out at Nanjing Hongchuang Geological Exploration Technology Service Co., Ltd., using a Neptune XT model MC - ICP-MS instrument. The analysis process was equipped with a signal smoothing device to improve signal stability and isotopic ratio measurement precision. Helium gas was used as the carrier gas, and a small amount of nitrogen gas was introduced after ablation to enhance the sensitivity of Hf elements. The combination of X skimmer cone and Jet sampling cone under the condition of adding a small amount of nitrogen gas could respectively increase the sensitivity of Hf, Yb, and Lu by 5.3 times, 4.0 times, and 2.4 times. The laser output energy could be adjusted, with an actual output energy density of 7.0 J/cm^2. The single-point ablation mode was employed, with a spot size fixed at 44 μm. Standard zircon 91500 was used for isotopic fractionation correction, with $^{176}Hf/^{177}Hf$ and $^{176}Lu/^{177}Hf$ ratios of 0.282785 and 0.0336, respectively. The selection and calculation of other Lu-Hf isotope constants are referred to Zhang et al. (2018).

3.2.2 Whole rock major, trace, and rare earth element analysis

Fresh samples of monzogranite and syenogranite were selected, crushed to 200 mesh without contamination, and then sent for analysis. Major element analysis involved washing and drying the samples with distilled water, followed by the preparation of lithium borate pellets after FeO titration and high-temperature heating. Analysis was conducted using an X-ray fluorescence spectrometer (XRF) in the laboratory, with an analysis error of less than 1%.Trace element analysis, including rare earth elements, involves a series of processes such as purification, drying, acidification, and dilution. Analysis was performed using an inductively coupled plasma-mass spectrometer (ICP-MS) in the laboratory, with an analysis error of less than 5%. All experimental work was conducted in the laboratory of the Hebei Institute of Regional Geology and Mineral Exploration.

4 Test results

4.1 Zircon U-Pb isotopic ages

The CL images of zircons reveal that both the monzogranite and syenogranite samples exhibit short-prismatic to columnar zircon shapes, with most zircons displaying clear oscillatory zoning and bright-dark oscillatory zoning structures (Figure 3A). These features indicate zircon characteristics formed during magmatic crystallization processes. The Th/U ratios of zircons in the monzogranite and syenogranite samples range from 0.39 to 0.57 and from 0.40 to 0.78 (with exceptions for individual points), respectively, confirming their magmatic origin. In the monzogranite samples, zircon grains have lengths ranging from approximately 80–120 μm, with length-to-width ratios of about 2:1 to 3:1. The $^{206}Pb/^{238}U$ concordant ages of 24 measurement points range from 292 to 289 Ma (Supplementary Table S1), with a weighted mean age of 291.1 ± 1.1 Ma (MSWD = 0.029; N=24) (Figures 3B, C). For the syenogranite samples, zircon grains have lengths ranging from approximately 85–160 μm, with length-to-width ratios of about 2:1 to 3:1. The $^{206}Pb/^{238}U$ concordant ages of 32 measurement points range from 268 to 254 Ma (Supplementary Table S2), with a calculated weighted mean age of 260.8 ± 1.1 Ma (Figures 3D, E; MSWD = 2.2; N=32) (Figures 3D, E).

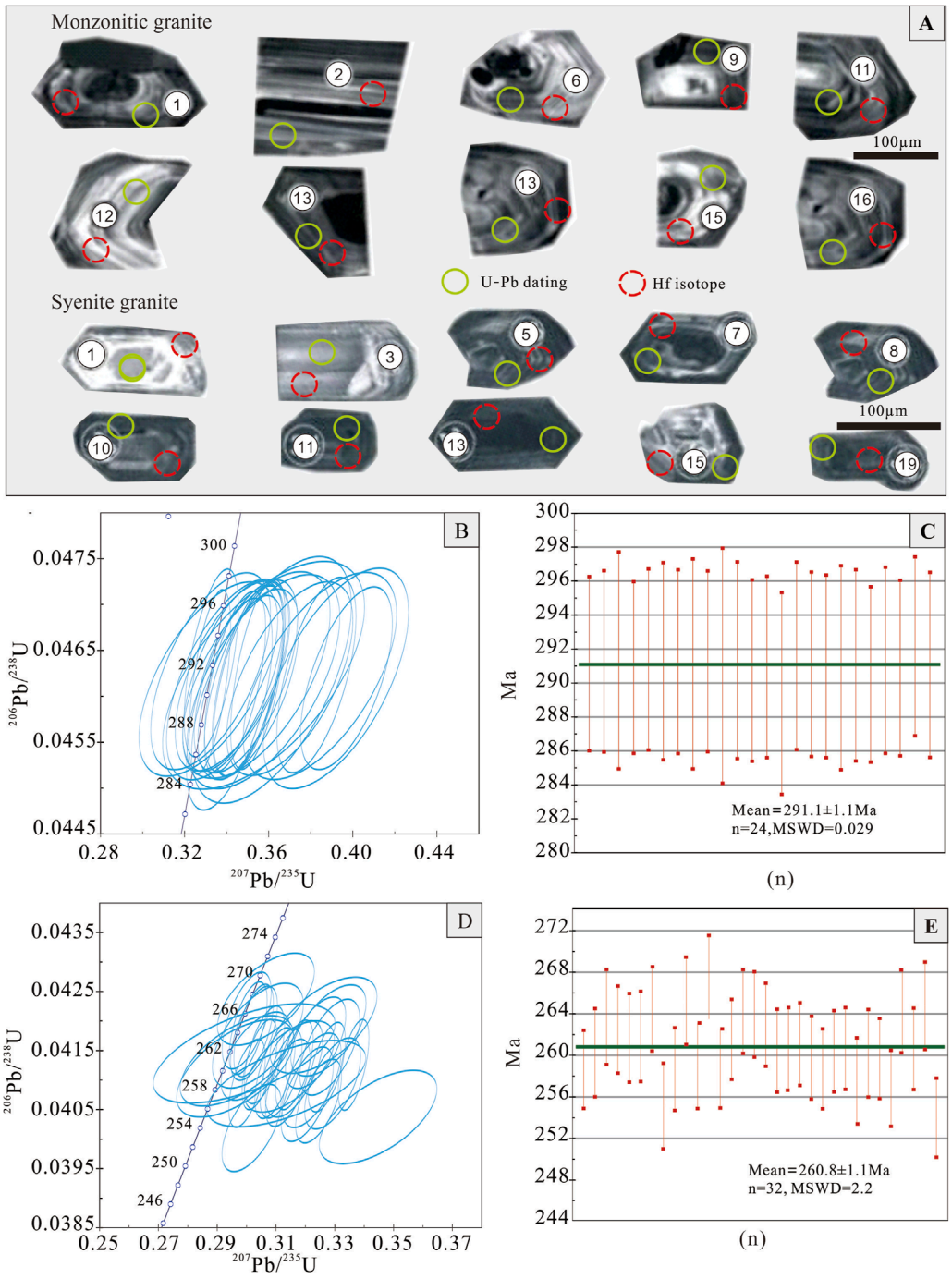

FIGURE 3
(A) Representative zircon CL images of diorite and syenogranite; **(B)** Zircon U-Pb Harmony Diagram of Erchang Granite; **(C)** Weighted average age map of diorite granite; **(D)** Zircon U-Pb Harmony Diagram of syenogranite; **(E)** Weighted average age map of syenogranite.

4.2 Whole rock major and trace element composition

The whole rock major and trace element composition are given in Supplementary Table S3, it can be observed that the monzogranite has relatively high SiO_2 content (74.10–76.06 wt%), K_2O content (4.42–4.48 wt%), Na_2O content (3.60–4.10 wt%), and total alkali content (Na_2O+ K_2O = 8.02–8.58 wt%), with low MgO (0.07–0.19 wt%), Fe_2O_3 (0.40–0.51 wt%), and FeO (0.38–0.53 wt%) as characteristics. On the (Na_2O+ K_2O) - SiO_2 diagram, the composition falls within the granite range and the sub-alkaline rock series area (Figure 4A); on the SiO_2 - K_2O diagram, the composition points fall into the high potassium calc-alkaline series (Figure 4B); on the Na_2O- K_2O alkalinity classification diagram, the composition

points fall into the potassic rock series area (Figure 4C); on the A/NK - A/CNK diagram, they fall into the peraluminous area (Figure 4D). Regarding rare earth elements, the whole-rock ΣREE is (119.35–146.98) × 10^{-6}, with light rare earth elements LREE/HREE = 11.39–13.65, $(La/Yb)_N$ = 12.47–16.43, δEu = 0.69–0.75, showing weak negative Eu anomalies and moderate fractionation right inclined form on the rare earth distribution curve (Figure 4E); $(La/Sm)_N$ is 5.83–6.90, $(Gd/Yb)_N$ is 1.37–1.53, indicating a certain degree of fractionation of light rare earth elements internally and a low degree of fractionation of heavy rare earth elements. The obtained whole-rock trace element characteristics indicate obvious enrichment of large ion lithophile elements such as Rb, Th, U, K, and relative depletion of elements such as Ba, Sr, Nb, Ti, and P (Figure 4F).

The syenogranite exhibits high contents of SiO2 (73.65–78.2 wt%), Al_2O_3 (12.23–13.95 wt%), K_2O (4.55–5.94 wt%), Na_2O (3.05–3.46 wt%), and total alkali (K_2O+ Na2O = 7.60–9.40 wt%), along with relatively low contents of MgO (0.10–0.18 wt%), CaO (0.17–0.26 wt%), MnO (0.01–0.02 wt%), P_2O_5 (0.01–0.02 wt%), and TiO_2 (0.05–0.18 wt%). It falls within the subalkaline granite field (Figure 4A), transitioning between high-K calc-alkaline and shoshonitic rocks (Figure 4B), or between potassic and high-potassic rocks (Figure 4C), and represents metaluminous rocks (Figure 4D). In terms of rare earth elements, most samples exhibit relatively high total rare earth element concentrations (ΣREE = 214.87–325.92 × 10^{-6}), relatively low LREE/HREE ratios (2.54–6.41), (La/Yb)N ratios (3.57–7.64), and low (La/Sm)N (1.51–3.90), (Gd/Yb)N ratios (0.46–2.08), as well as low δEu values (0.04–0.15), showing a strong negative Eu anomaly in a "V"-shaped or "four-component effect" distribution pattern (Wu et al., 2007) (Figure 4E). In terms of trace elements, it is enriched in large ion lithophile elements such as Rb, Th, and K, while exhibiting strong depletion in elements like Ba, Sr, Nb, Ta, Ti, and P (Figure 4F).

The syenogranite exhibits high contents of SiO_2 (73.65–78.2 wt%), Al_2O_3 (12.23–13.95 wt%), K_2O (4.55–5.94 wt%), Na_2O (3.05–3.46 wt%), and total alkali (K_2O+ Na_2O = 7.60–9.40 wt%), along with relatively low contents of MgO (0.10–0.18 wt%), CaO (0.17–0.26 wt%), MnO (0.01–0.02 wt%), P_2O_5 (0.01–0.02 wt%), and TiO_2 (0.05–0.18 wt%). It falls within the subalkaline granite field (Figure 4A), transitioning between high-K calc-alkaline and shoshonitic rocks (Figure 4B), or between potassic and high-potassic rocks (Figure 4C), and represents metaluminous rocks (Figure 4D). In terms of rare earth elements, most samples exhibit relatively high total rare earth element concentrations (ΣREE = 214.87–325.92 × 10^{-6}), relatively low LREE/HREE ratios (2.54–6.41), $(La/Yb)_N$ ratios (3.57–7.64), and low $(La/Sm)_N$ (1.51–3.90), $(Gd/Yb)_N$ ratios (0.46–2.08), as well as low δEu values (0.04–0.15), showing a strong negative Eu anomaly in a "V"-shaped or "four-component effect" distribution pattern (Wu et al., 2007) (Figure 4E). In terms of trace elements, it is enriched in large ion lithophile elements such as Rb, Th, and K, while exhibiting strong depletion in elements like Ba, Sr, Nb, Ta, Ti, and P (Figure 4F).

4.3 Hf isotopes

For the monzogranite, there are a total of 16 Hf isotope measurement points corresponding to single-grain zircon U-Pb dating (Supplementary Table S4). The data show that $^{176}Lu/^{177}Hf$ ranges from 0.000916 to 0.001838, and $^{176}Hf/^{177}Hf$ ranges from 0.282717 to 0.282794. The corresponding εHf(t) values vary from +4.1 to +7.0 (all greater than 0). The corresponding zircon T_{DM1} ranges from 576 to 495 Ma, which is significantly less than the second-stage model age T_{DM2} of 1130 to 920 Ma. For the syenogranite, the data from 13 zircon grains *in situ* Hf measurement points show that $^{176}Lu/^{177}Hf$ ranges from 0.000870 to 0.002562, and $^{176}Hf/^{177}Hf$ ranges from 0.282647 to 0.282859. The corresponding εHf(t) ranges from +0.8 to +8.6. T_{DM1} ranges from 894 to 561 Ma, significantly less than the second-stage model age $T_{DM2}$of to 1228 to 738 Ma (Supplementary Table S5). The composition points of both types of granites fall on the crustal (1 Ga evolution line) on the t (Ma) - εHf(t) plot (Figure 5A). On the t (Ma) - $^{176}Hf/^{177}Hf$ plot, the composition points fall between the depleted mantle and lower crust (Figure 5B).

5 Discussion

5.1 Petrogenesis and source characteristics

Granites are typically classified into three main genetic types: S-type, I-type, and A-type, which are formed by magmatic processes in corresponding tectonic environments and source regions during geological periods (Patio Douce, 1997; Sun and Yang, 2009). Geochronological and major element geochemical characteristics indicate that there is a 30 Ma difference in the formation ages between the monzogranite and syenogranite. Moreover, the linear relationships between SiO_2 (73.65%–78.26%) and other major elements such as MgO, Al_2O_3, CaO, Na_2O, K_2O, TiO_2, and P_2O_5 are not significant (refer to Figure 6), indicating that they do not share the same source or synchronous magmatic activity, and exhibit relatively independent magmatic characteristics. Therefore, the following discussion will focus on the petrological, lithological, and elemental geochemical characteristics from field geology, lithology, and elemental geochemistry perspectives, respectively.

5.1.1 Petrogenesis and source characteristics of monzogranite

Geological and lithological features indicate that the monzogranite occurs as irregular intrusive bodies with a medium-grained granitic structure, suggesting it is a medium to deep-seated intrusive rock. The rock-forming minerals include plagioclase, orthoclase, quartz, and accessory minerals such as apatite, zircon, and magnetite. It is characterized by relatively high SiO_2 (74.10–6.06 wt%), CaO (0.43–0.80 wt%), and Na_2O (3.6–4.1 wt%) contents, low P_2O_5 content, and features such as K_2O/Na_2O and Fe_2O_3/FeO ratios (refer to Figures 6A, B, D). The aluminum saturation index (A/CNK (Al_2O_3/(CaO + Na_2O+ K_2O)) is greater than 1.1, indicating the geochemical characteristics of "I-type granites." On the (Zr+Nb+Ce+Y)-(Na_2O+K_2O)/CaO diagram, the compositional points fall within the high fractionation I-type granite (GF) region (Figure 7A). Similarly, on the 100 ∗ ($MgO+FeO^T+TiO_2$)/SiO_2-(Al_2O_3+CaO)/(FeO^T+K_2O+Na_2O) diagram, the compositional points also fall within the high fractionation I-type granite and calc-alkaline rock areas (Figure 7B). Moreover, on the I-type and

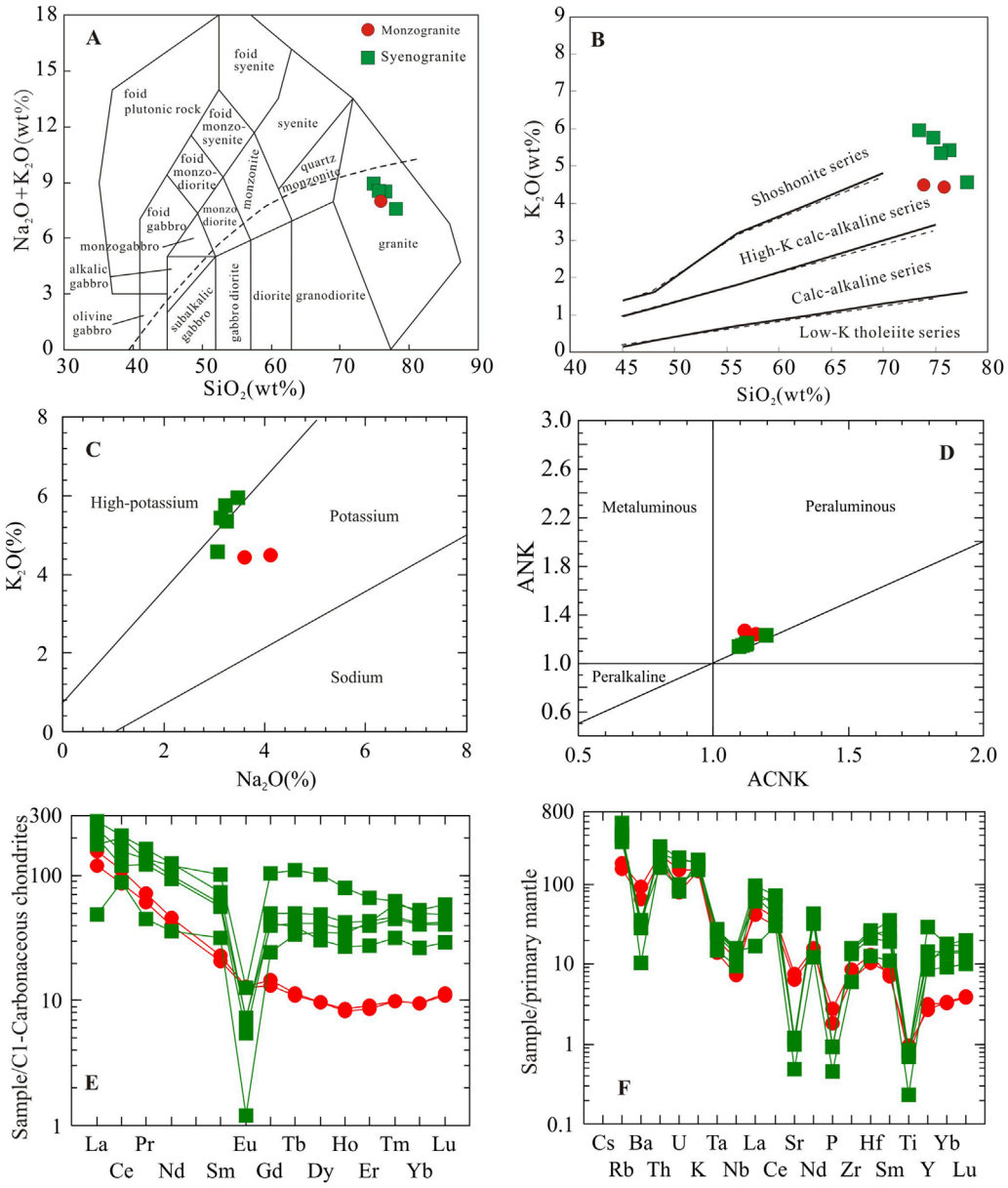

FIGURE 4
(A) Classification diagram of magmatic rocks (Na2O+K2O) - SiO2 (TAS) (Middlemost, 1994); **(B)** K2O-SiO2 diagram (Peccerillo and Taylor, 1976; Middlemost, 1985); **(C)** Classification map of Na2O K2O alkaline substances in rocks; **(D)** Graphical discrimination of granite A/NK-A/CNK (Maniar and Piccoli, 1989); **(E)** Standardized distribution diagram of rare earth element chondrite (Sun and McDonough, 1989); **(F)** Raw mantle standardization spider web diagram of trace elements (raw mantle standardization data according to Sun and McDonough, 1989).

S-type evolutionary diagrams, they tend to exhibit characteristics of I-type granites (Figures 7C, D). Considering the trend of decreasing P_2O_5 content with increasing SiO_2 content, the monzogranite is inferred to be I-type highly fractionated granite. This is because typical S-type granites have phosphate minerals that can be dissolved in strongly peraluminous melts, leading to an increase in P_2O_5 content during fractional crystallization (Chappell and White, 2001). The Sr content ranges from 134.10 to 158.60×10^{-6}, Y content ranges from 12.22 to 14.38×10^{-6}, and Yb content ranges from 1.62 to 1.63×10^{-6}, characteristic of low Sr and low Yb granite types. In terms of magma properties, the monzogranite has relatively low K_2O/Na_2O (1.09–1.23) and Fe_2O_3/FeO (0.11–0.96) ratios, indicating it crystallized from relatively reducing high-potassium calc-alkaline magma (Figures 6A, B).

The enrichment of large ion lithophile elements such as Rb, Th, U, and K, coupled with the depletion of elements like Ba, Sr, Nb, Ti, and P (refer to Figures 4E, F), is attributed to both magmatic crystallization differentiation and source region characteristics, as well as partial melting processes (Rudnick and Gao, 2003). Specifically, the depletion of Ba and Sr is related to plagioclase fractionation during magmatic processes or residual components in the source region. The relative depletion of P and Ti is associated

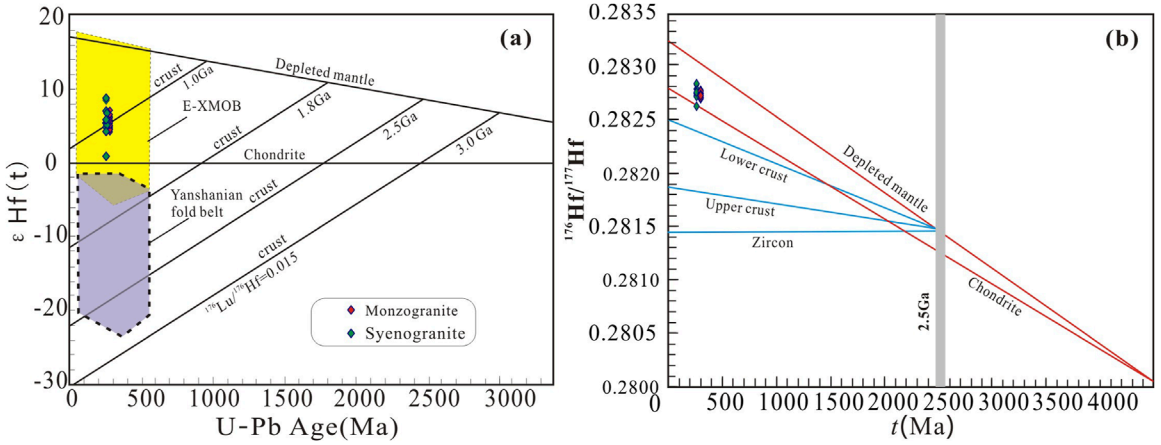

FIGURE 5
Hf isotope diagram of zircon (Vervoort et al., 1996; Yang et al., 2006).

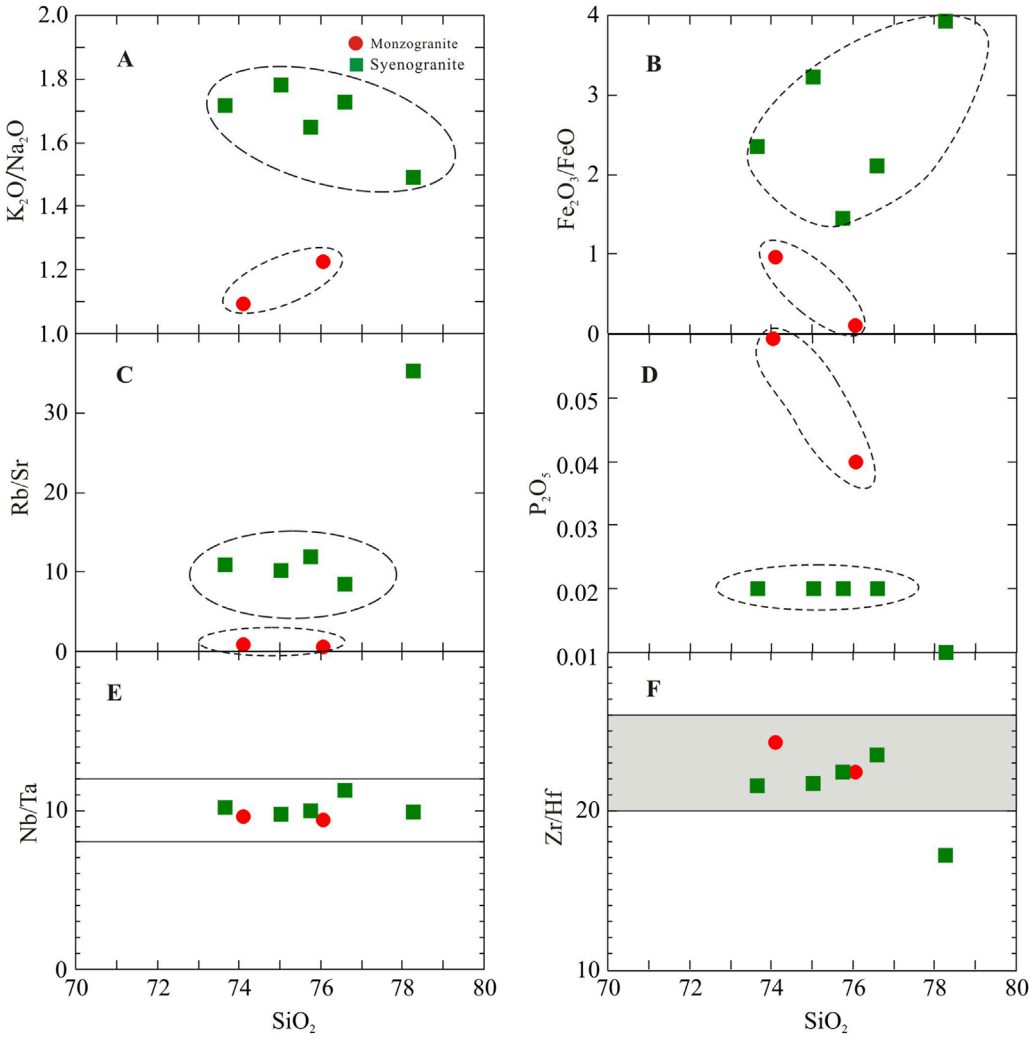

FIGURE 6
Diagram of the relationship between whole rock SiO_2 and related oxides and element ratios.

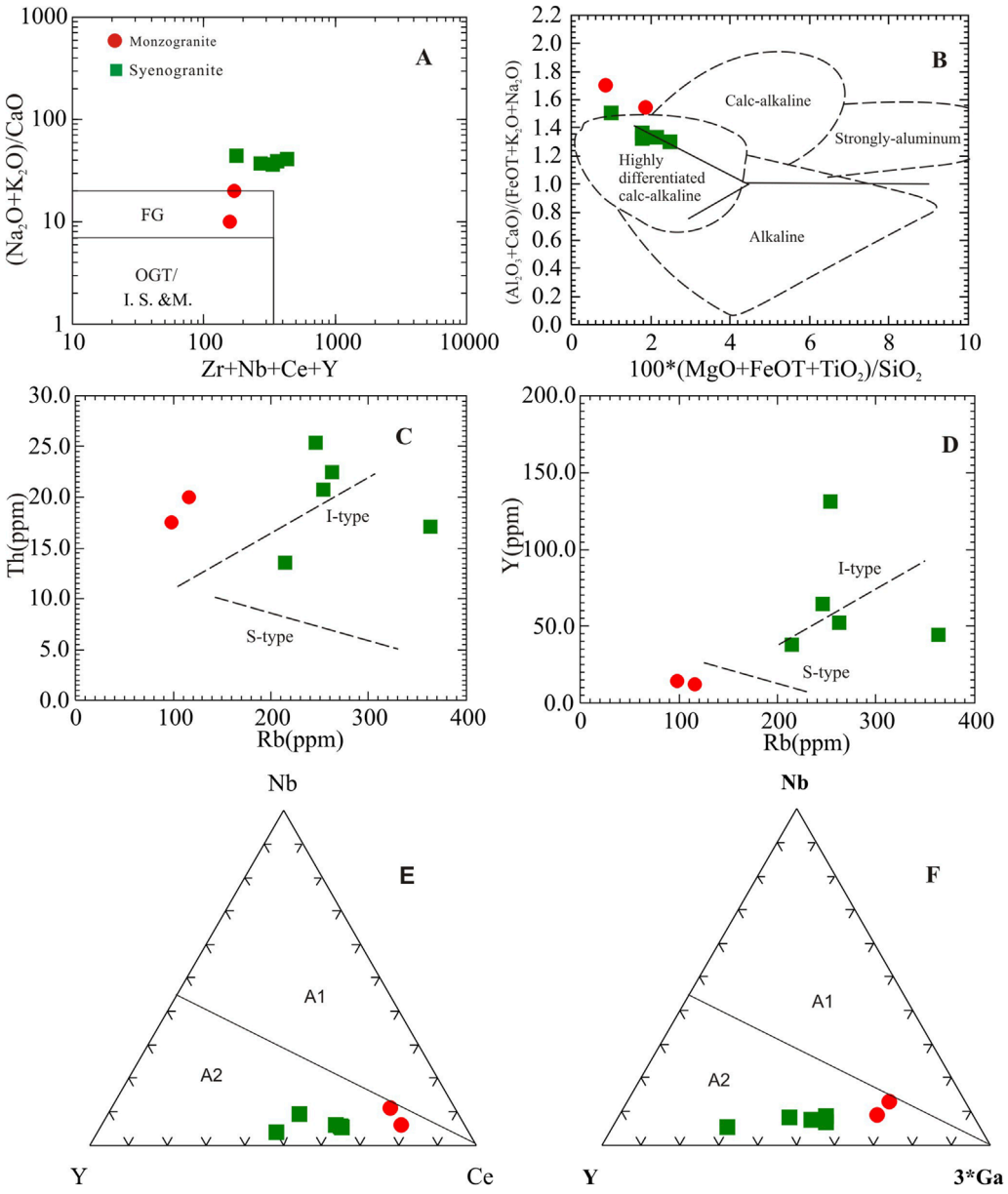

FIGURE 7
Diagram for distinguishing the genetic types of diorite granite and syenite granite.

with the crystallization and separation of accessory minerals such as apatite and ilmenite during magmatic processes (Figure 4F). The negative anomalies of Nb and Ta, along with Nb/Ta ratios ranging from 9.39 to 9.64, suggest the occurrence of fractional crystallization during the magma processes or an enriched mantle source (EMII) or fluid metasomatism of the lower crust dominated by water-rich fluids (lower crust Nb/Ta = 10; upper crust Nb/Ta = 11.36).

Numerous studies have demonstrated that I-type granites can form through various magmatic processes, including crystallization differentiation of mantle-derived magmas (with or without assimilation of crustal material), partial melting of crustal material in the deep or shallow crust, and mixing of mantle-derived and crustal melts (Xie et al., 2021). Combining the aforementioned features with the characteristics of low Mg (MgO = 0.07–0.19 wt%), low Fe (Fe_2O_3 = 0.04–0.51 wt%; FeO = 0.38–0.53 wt%), and low Co (0.78–0.61×10^{-6}), Cr (23.79–24.12×10^{-6}), indicates that the magma is unlikely to have originated from mantle-derived magmas through crystallization differentiation (Bonin, 2007), but rather exhibits characteristics more consistent with crustal rocks. The Hf isotope characteristics show that the εHf(t) values of zircons in the monzogranite range from +4.1 to +7.0 (all greater than 0), corresponding to T_{DM1} values of 561–894 Ma and T_{DM2} values of 920–1130 Ma. On the source discrimination diagrams, the compositional points fall near the Late Paleozoic Xing'an-Mongolian Orogenic Belt or its eastern segment (CAOB) or around the average crustal evolution line of 1.0 Ga (Figure 5A), and between the

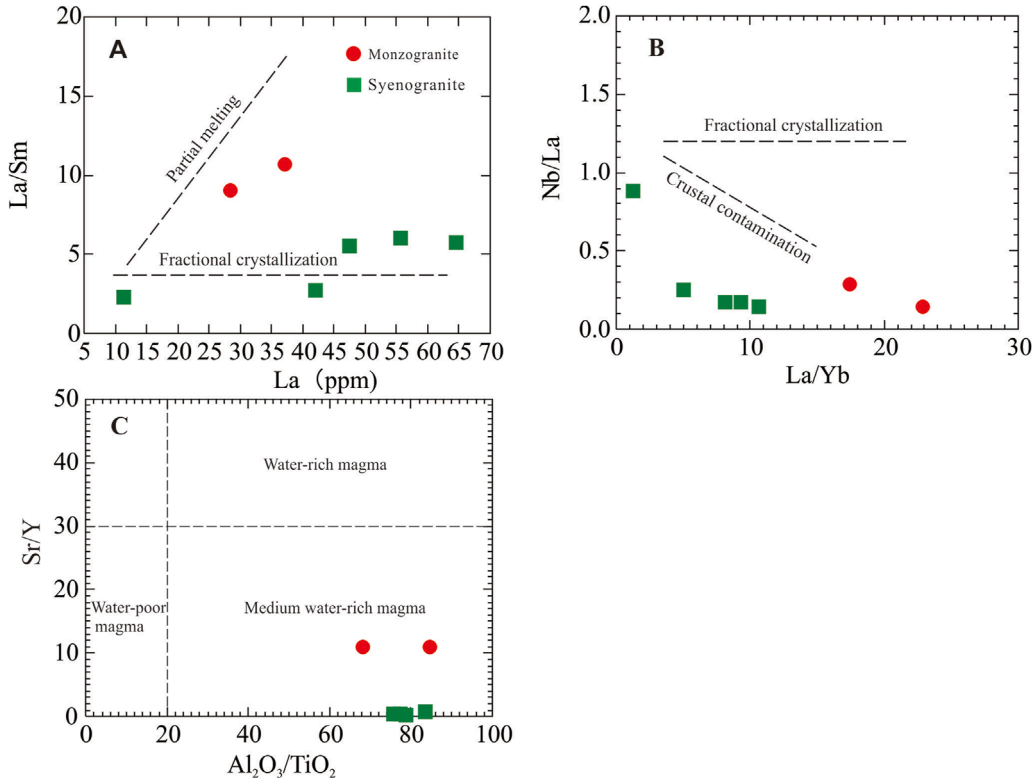

FIGURE 8
Diagram of the relationship between magma evolution, formation pressure, and water content. Note: According to literature Loucks, 2014; **(B–C)** base images according to literature Pearce et al., 1984.

depleted mantle and lower crust (Figure 5B), suggesting that the magma may have originated from newly formed young lower crust or partial melting of Mesoproterozoic lower crust. The Nb/Ta ratio is 9.39–9.64 (similar to Nb/Ta ratios in residual hornblende and garnet-bearing granites, which is ~9), indicating the presence of residual hornblende and garnet in the source region, with magma evolution dominated by fractional crystallization and minor crustal contamination (Figures 8A, B).

In terms of the physical and chemical characteristics of the magma and source region, the results of zircon saturation temperature calculations indicate that the magma of the monzogranite approached temperatures of 730°C–755°Cat emplacement or should have formed at temperatures greater than 755°C (calculated using the formula by Watson and Harrison, 1983). On the Al_2O_3/TiO_2-Sr/Y simulation diagram, the compositional points fall in a moderate to relatively high water area (Figure 8C). It holds relatively low K_2O/Na_2O (1.09–1.23) and Fe_2O_3/FeO (0.11–0.96) ratios, indicating that the magma exhibits relatively reducing properties and is relatively rich in potassium (Figures 6A, B). The Zr/Hf ratio ranges from 22.37 to 24.24, which is generally lower than the values found in typical granites (39–36), and approaches the chondrite value of 38, and is lower than the average value of 25 in granodiorite (107 samples). The relatively low Zr/Hf ratio suggests that the crystallization of zircon to some extent inhibits the strong enrichment of Zr and Hf in the magma, indicating a relatively low degree of involvement of fluids. Therefore, it further indicates that this type of magma is high-differentiated I-type granite, with magma evolution primarily controlled by the crystallization differentiation of minerals such as plagioclase (biotite, etc.), zircon, apatite, and garnet (Stepanov et al., 2014), with minor contamination by crustal material.

5.1.2 The origin and source characteristics of the syenogranite

The emplacement of the syenogranite occurred later than that of the monzogranite. Spatially, both constitute a complex granite body extending in a northeast direction, and the characteristics of medium-grained granite structures indicate that they are intrusive rocks formed at intermediate to deep levels. The primary mineral phases include plagioclase, potassium feldspar, quartz, and biotite, with accessory minerals such as apatite, zircon, and magnetite. Its high SiO_2 content (73.65–78.26 wt%) and low concentrations of MgO (0.10–0.18 wt%), CaO (0.17–0.26 wt%), and P_2O_5 (0.01–0.02 wt%), along with an aluminum saturation index (A/CNK ($Al_2O_3/(CaO + Na_2O + K_2O)$) greater than 1.1, and a typical "four-component effect" in the distribution of rare earth elements, and strong depletions in Ba, Sr, P, Ti, etc., indicate its geochemical attributes as an "A-type granite" (Eby, 1992; Wu et al., 2007). Compositional points on the (Zr+Nb+Ce+Y)-(Na_2O+K_2O)/CaO diagram fall within the "A-type granite" (GF) region (Figure 7A), and on the $100 * (MgO+FeO^T+TiO_2)/SiO_2$-$(Al_2O_3+CaO)/(FeO^T+K_2O+Na_2O)$ diagram, they fall within

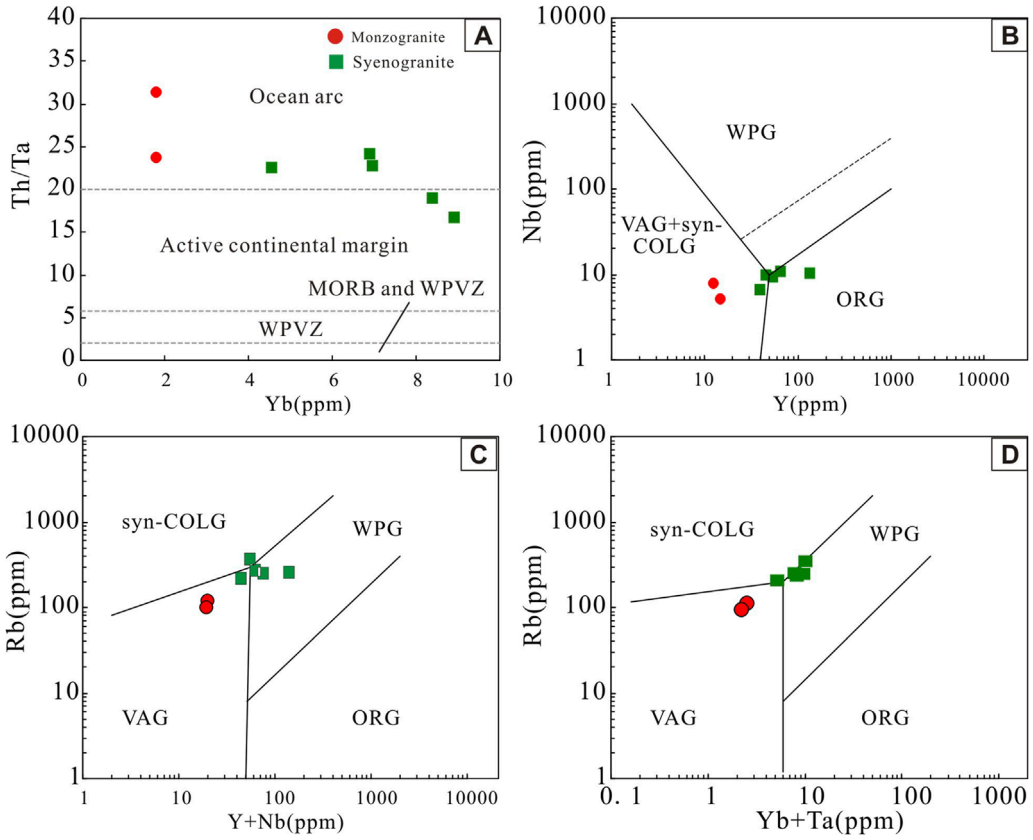

FIGURE 9
Tectonic environment identification diagrams based on trace element of intrusive rock samples in the study area (Gorton and Schandl, 2000; Pearce et al., 1984).

the calc-alkaline rock region (Figure 7B), consistent with the characteristics of the transition between high-potassium calc-alkaline series and potassium-bearing mafic rock series (Figure 4B). Although the trend in the I-type and S-type evolution diagrams leans towards the characteristics of I-type granite, and there is no significant change in P_2O_5 content with increasing SiO_2, the possibility of A-type granite genesis cannot be ruled out (Chappell and White, 2001).

In terms of the origin of A-type granite, it mainly includes extreme crystalline differentiation of mantle-derived magma, partial melting of crustal rocks (such as metamorphic sedimentary rocks or mafic granulite lower crust), decompression melting of felsic rocks in the upper crust, and mixing of mantle melts with deep-seated granite melts (Eby, 1992; Patino Douce, 1997; Bonin, 2007). The major element analysis of the syenogranite in this study shows higher SiO_2 content and lower MgO content, while trace element testing results reveal low levels of Cr (18.70–25.04 $\times10^{-6}$), Co (0.76–2.38 $\times10^{-6}$), and V (12.37–33.34 $\times10^{-6}$), which are significantly different from granites formed by mantle-derived magma differentiation, indicating it is unlikely to be derived from mantle-derived magma differentiation (Bonin, 2007; Wu et al., 2007). Additionally, the study area and adjacent areas in the Early to Middle Permian only have a small amount of gabbro (Liu J. F. et al., 2022). The strong depletion of Ba, Sr, P, Ti, and the high K_2O/Na_2O, Rb/Sr ratios suggest that the magma is more likely to be derived from partial melting of the crustal source. In terms of zircon Hf isotopes, the εHf(t) values of the syenogranite range from +4.2 to +8.6 (all greater than 0), corresponding to TDM_1 ages of 894–561 Ma and TDM_2 ages of 984–738 Ma. On the source discrimination diagram, the composition points are all located between the Late Paleozoic Xing'an-Mongolian Orogenic Belt or its eastern segment (CAOB) and the average evolution line of continental crust (1.0 Ga) (Figure 5A), and between the depleted mantle and the lower crust (Figure 5B), indicating that the magma originated from the newly generated young lower crust or the partially melted Mesoproterozoic lower crust (Wu et al., 2007). At the same time, the syenogranite is characterized by high alkaline (Na_2O+K_2O=7.604–9.398), indicating a contribution of mantle derived-melts (Depaolo, 1981). The εHf(t) values of syenogranite show both higher and lower components, indicating the involvement of minor mantle-derived fluids and crustal materials. The magmatic evolution process is dominated by fractional crystallization, with a minor contribution from crustal material contamination (Figures 8A, B).

In terms of physical and chemical characteristics, the zircon saturation temperature calculations indicate that the magma of the syenogranite began to approach temperatures of 734°C–802°C (as above) or formed at temperatures greater than 802°C. On the Al_2O_3/TiO_2-Sr/Y simulation diagram, the composition points are located in a relatively water-deficient state (Figure 8C). This is consistent with the characteristics of a low Sr, high Yb-type granite

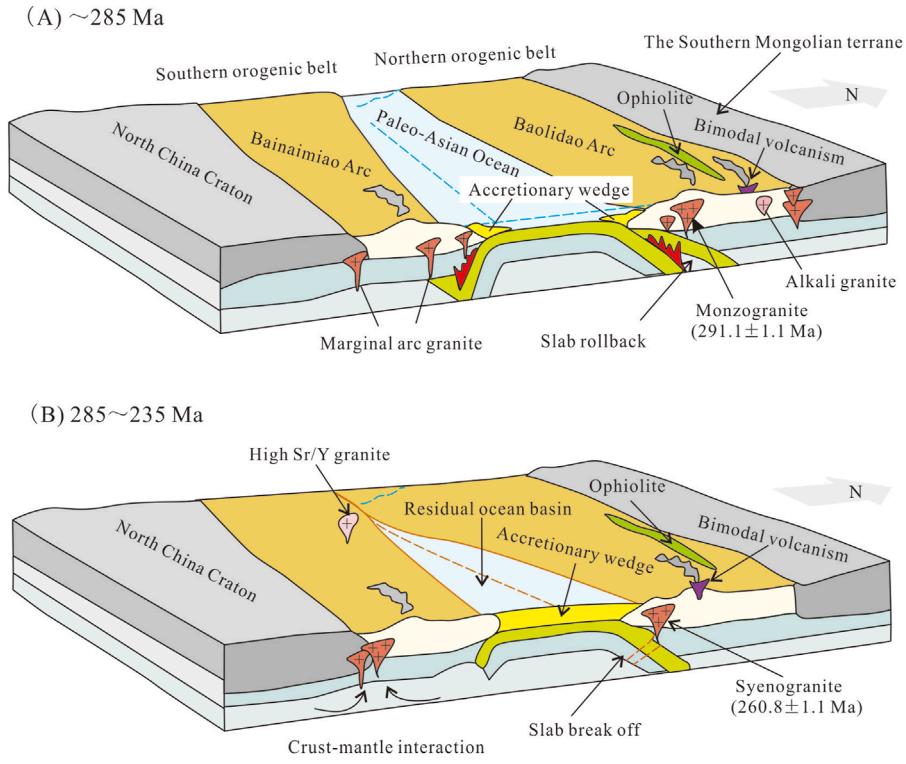

FIGURE 10
Schematic diagram of monzogranite **(A)** and syenogranite **(B)** tectono-magmatic evolution (modidied after Wu et al., 2021).

reflected by its high Y (38.32–131.30 $\times10^{-6}$), Yb (4.46–8.96 $\times10^{-6}$), and low Sr (10.28–25.45 $\times10^{-6}$), $(La/Yb)_N$ ratio (0.86–7.18), and Sr/Y ratio (0.19–0.66), indicating that the initial magma formation occurred in a low-pressure environment with no residual garnet in the source area. The syenogranite holds a relatively high K_2O/Na_2O (1.09–1.23) and Fe_2O_3/FeO (0.11–0.96) ratio, indicating its magma has a relatively sodium-rich oxidizing property (Figures 6A, B). The Zr/Hf ratio ranges from 17.17 to 23.47, which is generally lower than the typical granite range of 36–39 and closer to the chondrite value of 38, and is also consistent with the low Zr/Hf ratio found in granites, indicating that zircon crystallization has to some extent prevented strong enrichment of Zr and Hf in the magma, and the involvement of fluids in the process is relatively low. This feature aligns with the anhydrous nature of "A-type" granite as defined in previous studies (Eby, 1992; Patino Douce, 1997), while also ruling out the possibility of partial melting of the lower crust granulite phase. Additionally, the syenogranite exhibits a significant negative Eu anomaly in its rare earth element distribution pattern, indicating that the magma evolution process is unlikely to have involved significant plagioclase crystallization separation and possibly had constraints from residual sources in the source area. Furthermore, the depletion of Nb and Ta and the Nb/Ta ratio of 9.47–11.27 suggests the presence of residual minerals such as rutile and ilmenite in the source region.

In terms of magma evolution, considering that the adiabatic ascent intrusion temperature of granitic magma exceeds 802°C, according to the normal geothermal gradient, it may be difficult for the shallow crust to reach such high melting temperatures. Therefore, the magma of the syenogranite is likely to have formed by partial melting of the Mesoproterozoic lower crust, rapidly intruding and crystallizing during crustal thinning processes. Furthermore, its whole-rock Nb/Ta ratio (9.88–11.27) is close to the crustal value (11; according to Green, 1995), and the Zr/Hf ratio (17.17–23.47) is similar to that of the monzogranite, indicating their consanguinity. The high Rb/Sr ratio characteristic (10.22–35.28) is influenced by the high degree of crustal material contamination. In other words, the syenogranite is produced by partial melting of the Mesoproterozoic lower crust, with residual minerals such as plagioclase, amphibole, and garnet, and it exhibits both relatively high and low Hf isotopic signatures, suggesting contamination of mantle and crustal material (Figure 7).

5.2 Geodynamic setting

The tectonic evolution of the northern margin of the North China Craton is characterized by multiple magmatic events from the Late Paleozoic to the Early-Middle Triassic, corresponding to the evolution of the Paleo-Asian Ocean (Xing, 2022). Regarding the relationship between granite genesis and the Xing'an - Mongolia Orogenic Belt, it is observed that the formation of collision-related S-type granites in eastern Inner Mongolia and the middle segment of the northern margin of the North China Craton occurred during the Late-Middle Permian to Triassic, suggesting that the closure of the Paleo-Asian Ocean lasted until at least the Triassic (Chen, 2018). In terms of stratigraphic research, it is noted that the entire plant fossil assemblage of the Jiabeigou Formation in the Middle

Permian belongs to the Huaxia Flora, while the lower part of the Linxi Formation in the Late Permian represents typical marine deposits, transitioning to typical continental deposits in the upper part. Paleogeographic reconstructions of the southern segment of the Greater Khingan Range indicate residual basin settings during the Early-Middle Permian, transitioning to fluvial-lacustrine deposits during the Triassic, suggesting that the closure of the Paleo-Asian Ocean did not occur until the Early-Middle Permian. This is indicative of the bidirectional subduction of Paleo-Asian oceanic plates beneath the southern part of the Xing'an orogenic belt and the northern margin of the North China Craton (Sun et al., 2016). Additionally, well-preserved Permian-Triassic sedimentary sequences in the Arukorqin Banner region further suggest that the closure of the Xing'an orogenic belt and the onset of continental collision occurred as early as the Late Permian and persisted into the Early Triassic (Zhang et al., 2022).

The zircon U-Pb geochronological study of the Jielin Ranch in this study reveals that the monzogranite was emplaced in the Early Permian (291.1 ± 1.1 Ma), while the syenogranite formed at the end of the Middle Permian (260.8 ± 1.1 Ma). Magmatic activity is closely related to the tectonic evolution of the Paleo-Asian Ocean and the Xing'an - Mongolia Orogenic Belt. Regarding the tectonic environment indicated by granite genesis, I-type granites typically form in island arc or continental margin settings. A-type granites, on the other hand, either form in intraplate non-orogenic settings (A_1), often exhibiting certain similarities to island arc basalts or in extensional environments resulting from the post-collisional extension caused by the slab rollback in subduction zones or the extensional settings associated with continental rifting (A_2) (Eby, 1992). The monzogranite at the Jielin Ranch studied in this study was formed in the Early Permian (291.1 ± 1.1 Ma), with Th/Ta ratios varying around 2. The syenogranite was formed at the end of the Middle Permian (260.8 ± 1.1 Ma), with Th/Ta >2, indicating characteristics of crustal evolution from continental margin arc to oceanic arc (Figure 9A). In the tectonic granite elemental discrimination diagrams (Figures 9B–D), the data points for the monzogranite fall along the boundary between the collision-related volcanic arc and the orogenic belt or the boundary within the plate, which may be experienced a subduction-compressional or extension tectonic environment (Acocella and Funiciello, 2010). On the other hand, the data points for the syenogranite fall within the collision-related volcanic arc or volcanic arc region. Moreover, the syenogranite Y/Nb ratios are between 4.434 and 12.364 (>1.2), which belong to A2-type granite (Eby, 1992) and in the diagram Nb-Y-Ce and Nb-Y-3Ga, the samples all plot in the A2 area (Figures 7E, F). Therefore, we proposed that the syenogranite belongs to A2-type granite, further supporting this conclusion. Hence, it can be inferred that the monzogranite (~291 Ma) in the Jielin Ranch area formed in an active continental margin environment, where partial melting of the mantle wedge induced by the dehydration of the subducted slab produced high-temperature mafic magma that intruded into and heated the crust, leading to partial melting (Figure 10A). The syenogranite (~261 Ma) likely formed in a post-subduction extensional setting of the Paleo-Asian Ocean, associated with active continental margin tectonic environments such as oceanic ridge subduction (during which slab windows may have appeared and rifted), slab rollback, detachment, or extension (Figure 10B). This oceanic ridge subduction related slab rollback and extension model can also be widely insight from the eastern Pacific where oceanic ridges subducted beneath both north (i.e., Yukon Triple Junction, Mendocino Triple Junction, and Rivera Triple Junction) and south (i.e., Panama Triple Junction and Chile Rise) American blocks (Sisson and Pavlis, 1993; Windley and Xiao, 2018).

6 Conclusion

This study traces the geological, petrographic, zircon U-Pb chronology, Hf isotope, and petrochemical characteristics of the Permian granitoid rocks developed in the JielinRanch area, the east of Xilingol League, Inner Mongolia. The preliminary understandings obtained are as follows.

(1) The granitoid rocks in the JielinRanch area are composite rock bodies, and the petrographic phases are composed of monzogranite and syenogranite. The rock-forming ages are the Early Permian (291.1 ± 1.1 Ma) and the end of the Middle Permian (260.8 ± 1.1 Ma), respectively.

(2) The monzogranite belongs to the potassium-rich and high-K calc-alkaline rock series, exhibiting the characteristics of a highly fractionated "I-type" granite. The magma originated from the partial melting of the Meso-Neoproterozoic lower crust. The syenogranite is a transitional rock series from potassium-rich to high-K rocks, possessing the geochemical properties of "A_2-type" granite. The magma originated from the partial melting of the Meso-Neoproterozoic lower crust with the participation of mantle-derived melts, and a small amount of upper crustal material was added.

(3) Based on the analysis of regional geodynamic evolution characteristics, the study area experienced a volcanic arc environment in the early stage of the Xingmeng Orogenesis during the Early Permian, and a brief orogenic extension may have occurred in the late Middle Permian.

Data availability statement

The original contributions presented in the study are included in the article/Supplementary Material, further inquiries can be directed to the corresponding authors.

Author contributions

XX: Data curation, Writing–original draft. PZ: Methodology, Writing–original draft. GC: Formal Analysis, Writing–original draft. HZ: Software, Writing–original draft. XZ: Investigation, Writing–original draft.

Funding

The author(s) declare(s) that no financial support was received for the research, authorship, and/or publication of this article.

Acknowledgments

We express our gratitude to Chief editor Valerio Acocelle, Executive editor Dr Hongjian Zhu, and three reviewers for their constructive and valuable comments, which improved the quality of this study. This research was funded by the China Geological Survey project (No. 1212011120696), the Jilin Provincial Natural Science Foundation project (No. 20220101178JC), and the Changchun University of Engineering Doctoral Fund project.

Conflict of interest

The authors declare that the research was conducted in the absence of any commercial or financial relationships that could be construed as a potential conflict of interest.

Publisher's note

All claims expressed in this article are solely those of the authors and do not necessarily represent those of their affiliated organizations, or those of the publisher, the editors and the reviewers. Any product that may be evaluated in this article, or claim that may be made by its manufacturer, is not guaranteed or endorsed by the publisher.

Supplementary material

The Supplementary Material for this article can be found online at: https://www.frontiersin.org/articles/10.3389/feart.2024.1437599/full#supplementary-material

References

Acocella, V., and Funiciello, F. (2010). Kinematic setting and structural control of arc volcanism. *Earth Plan. Sci. Lett.* 289 (1-2), 43–53. doi:10.1016/j.epsl.2009.10.027

Bonin, B. (2007). A-type granites and related rocks: evolution of a concept, problems and prospects. *Lithos* 97 (1-2), 1–29. doi:10.1016/j.lithos.2006.12.007

Chappell, B. W., and White, A. J. R. (2001). Two contrasting granite types: 25 yearslater. *Aust. J. Earth Sci.* 48, 489–499. doi:10.1046/j.1440-0952.2001.00882.x

Chen, J. S. (2018). *Petrogenesis of the late paleozoic to early mesozoic granitic from the Chifeng region and their tectonic implication*. Ph.D. Dissertation. Changchun: Jilin University, 1–183. (in Chinese with English abstract).

DePaolo, D. L. (1981). Trace element and isotopic effects of combined wallrock assimilation and fractional crystallization. *Earth Plan. Sci. Lett.* 53, 189–202. doi:10.1016/0012-821x(81)90153-9

Eby, G. N. (1992). Chemical subdivision of the A-type granitoids: petrogenetic and tectonic implications. *Geology* 20, 641–644. doi:10.1130/0091-7613(1992)020<0641:csotat>2.3.co;2

Eizenhöfer, P. R., Zhao, G. C., Zhang, J., Han, Y. G., Hou, W. Z., Liu, D. X., et al. (2015). Geochemical characteristics of the Permian basins and their provenances across the Solonker Suture Zone: assessment of net crustal growth during the closure of the Palaeo-Asian Ocean. *Lithos* 224–225, 240–255. doi:10.1016/j.lithos.2015.03.012

Gorton, M. P., and Schandl, E. S. (2000). From continents to island arcs: a geochemical index of tectonic setting for arc–related and within–plate felsic to intermediate volcanic rocks. *Can. Mineral.* 38, 1065–1073. doi:10.2113/gscanmin.38.5.1065

Green, H. T. (1995). Significance of Nb/Ta as an indicator of geochemical processes in the crust-mantle system. *Chem. Geol.* 120, 347–359. doi:10.1016/0009-2541(94)00145-x

Hu, Z. C., Zhang, W., Liu, Y. S., Gao, S., Li, M., Zong, K. Q., et al. (2015). "Wave" signal smoothing and mercury removing device for laser ablation quadrupole and multiple collector ICP-MS analysis: application to lead isotope analysis. *Anal. Chem.* 87, 1152–1157. doi:10.1021/ac503749k

Jahn, B. M., Wu, F. Y., and Chen, B. (2000). Granitoids of the central asian orogenic belt and continental growth in the phanerozoic. *Earth Environ. Sci. Trans. R. Soc.* 91, 181–193. doi:10.1017/s0263593300007367

Kröner, A., Kovach, V., Belousova, E., Hegner, E., Armstrong, R., Dolgopolova, A., et al. (2014). Reassessment of continental growth during the accretionary history of the central asian orogenic belt. *Gondwana Res.* 25 (1), 103–125. doi:10.1016/j.gr.2012.12.023

Li, Y. J., Wang, G. H., Santosh, M., Wang, J. F., Dong, P. P., and Li, H. Y. (2020). Subduction initiation of the SE Paleo-Asian Ocean: evidence from awell preserved intra-oceanic forearc ophiolite fragment in central Inner Mongolia, North China. *Earth Planet Sci. Lett.* 535, 116087. doi:10.1016/j.epsl.2020.116087

Li, Y. J., Wang, J. F., Li, H. Y., and Dong, P. P. (2015). Recognition of meilaotewula ophiolite in XiUjimqinBanner, inner Mongolia. *Acta Petrol. Sin.* 31 (5), 1461–1470. (in Chinese with English abstract).

Liu, C. F., Xu, M. T., Zhou, Z. G., Wang, G. S., Wu, C., Zhu, Y., et al. (2018). Magmatic history during late carboniferous to early permian in the North of the central xing'an-Mongolia orogenic belt: a case study of the Houtoumiao pluton, inner Mongolia. *Int. Geol. Rev.* 60, 1918–1939. doi:10.1080/00206814.2017.1410731

Liu, J. F., Li, J. Y., Zhang, W. L., Zhang, J., Zhao, S., Yin, D. F., et al. (2022b). Newly discovered late Devonian and early carboniferous ophiolite fragments in the diyanmiaomelange in southeastern inner Mongolia: implications for the late paleozoic tectonic evolution of the southeastern central asian orogenic belt. *Lithos* 408-409, 106566. doi:10.1016/j.lithos.2021.106566

Liu, J. F., Li, J. Y., Zhao, S., Zhang, J., Zheng, R. G., Zhang, W. L., et al. (2022a). Crustal accretion and Paleo-Asian Ocean evolution during late Paleozoic-early mesozoic in southeastern central Asian orogenic belt: evidence from magmatism in Linxi-Dongwuqi area, southeastern inner Mongolia. *Acta Petrol. Sin.* 38 (8), 2181–2215. doi:10.18654/1000-0569/2022.08.02

Liu, Y. J., Li, W. M., Feng, Z. Q., Wen, Q. B., Neubauer, F., and Liang, C. Y. (2017). A review of the Paleozoic tectonics in the eastern part of central Asian orogenic belt. *Gondwana Res.* 43, 123–148. doi:10.1016/j.gr.2016.03.013

Loucks, R. R. (2014). Distinctive composition of copper-ore-forming arcmagmas. *Aust. J. Ear Sci.* 61, 5–16. doi:10.1080/08120099.2013.865676

Ma, Y. F., Liu, Y. J., Peskov, A. U., Wang, Y., Song, W. M., Zhang, Y. J., et al. (2022). Paleozoic tectonic evolution of the eastern central Asian orogenic belt in NE China. *China Geol.* 5, 555–578. doi:10.31035/cg2021079

Maniar, P. D., and Piccoli, P. M. (1989). Tectonic discrimination of granitoids. *Geol. Soc. Am. Bull.* 101, 635–643. doi:10.1130/0016-7606(1989)101<0635:tdog>2.3.co;2

Mao, J. W., Zhou, Z. H., Wu, G., Jiang, S. H., Liu, C. L., Li, H. M., et al. (2013). Metallogenic regularity and minerogenetic series of oredeposits in Inner Mongolia and adjacent areas. *Mineral. Deposits* 32 (4), 715–729. (in Chinese with English abstract).

Middlemost, E. A. K. (1985). *Magmas and magmatic rocks*. London: Longman, 1–266.

Middlemost, E. A. K. (1994). Naming materials in the magma/igneous rock system. *Earth-Sci Rev.* 37 (3-4), 215–224. doi:10.1016/0012-8252(94)90029-9

Patino Douce, A. E. (1997). Generation of metaluminous A-type granites by low-pressure melting of calc-alkaline granitoids. *Geology* 25, 743–746. doi:10.1130/0091-7613(1997)025<0743:gomatg>2.3.co;2

Pearce, J. A., Harris, N. B. W., and Tindle, A. G. (1984). Trace element discrimination diagrams for the tectonic interpretation of granitic rocks. *J. Petrol* 25 (4), 956–983. doi:10.1093/petrology/25.4.956

Peccerillo, R., and Taylor, S. R. (1976). Geochemistry of Eocene calc-alkaline volcanic rocks from the Kastamonu area, Northern Turkey. *Contrib. Mineral. Petrol* 58, 63–81. doi:10.1007/bf00384745

Rudnick, R. L., and Gao, S. (2003). "The composition of the continental crust," in *Treatise on geochemistry, V. 3, the crust*. Editors H. D. Holland, and K. K. Turekian (Oxford: Elsevier-Pergamon), 1–64.

Şengör, A. M. C., Natal'in, B. A., and Burtman, U. S. (1993). Evolution of the Altaid tectonic collage and Paleozoic crustal growth in Eurasia. *Nature* 364, 209–304.

Sisson, V. B., and Pavlis, T. L. (1993). Geologic consequences of plate reorganization: an example from the Eocene southern Alaska forearc. *Geology* 21, 913–916. doi:10.1130/0091-7613(1993)021<0913:gcopra>2.3.co;2

Song, S. G., Wang, M. M., Xu, X., Wang, C., Niu, Y. L., Allen, M. B., et al. (2015). Ophiolites in the Xing'an-Inner Mongolia accretionary belt of the CAOB: implications for two cycles of seafloor spreading and accretionary orogenic events. *Tectonics* 34, 2221–2248. doi:10.1002/2015tc003948

Stepanov, A., Mavrogenes, J. A., Meffre, S., and Davidson, P. (2014). The keyrole of mica during igneous concentration of tantalum. *Contrib. Mineral. Petrol* 167 (6), 1009. doi:10.1007/s00410-014-1009-3

Sun, L. X., Zhang, Y., Li, Y. F., Xu, F., and Ren, B. F. (2020). Zircon U-Pb age and geochemistry of the Mesoproterozoic gneissic granite from Abaga Banner, Inner Mongolia and its tectonic significances. *Acta Petrol. Sin.* 36 (3), 781–798. (in Chinese with Englishabstract). doi:10.18654/1000-0569/2020.03.09

Sun, S. S., and Mcdonough, W. F. (1989). Chemical and isotopic systematics of oceanic basalts: implications for mantle composition and processes. *Geol. Soc. Spe. Pub* 42, 313–345. doi:10.1144/gsl.sp.1989.042.01.19

Sun, Y. W., Ding, H. S., Liu, H., Zhang, D. J., Gong, F. H., and Zheng, Y. J. (2016). Fossil plants from the Guadalupian Yujiabeigou Formation in thenorthern margin of North China plate and their tectonic implications. *J. Jilin Univ. (Earth Sci. Edi)* 46 (5), 1268–1283. (in Chinese with English abstract). doi:10.13278/j.cnki.jjuese.201605101

Tianjin Institute of Geological Survey (2014). *1:50000 L50E022011, L50E022012, L50E023011, L50E023012*. Tianjing: L50E024011 Regional Geological survey, Inner Mongolia Autonomous Region, 1–350. (in Chinese).

Vervoort, J. D., Patchett, P. J., Gehrels, G. E., and Nutman, A. P. (1996). Constraints on early Earth differentiation from hafnium and neodymium isotopes. *Nature* 379 (6566), 624–627. doi:10.1038/379624a0

Watson, E. B., and Harrison, T. M. (1983). Zircon saturation revisited: temperature and composition effects in a variety of crustal magma types. *Earth Planet Sci. Lett.* 64, 295–304. doi:10.1016/0012-821x(83)90211-x

Wilde, S. A. (2015). Final amalgamation of the central Asian orogenic belt in NE China: Paleo-Asian Ocean closure versus Paleo-Pacific plate subduction: a review of the evidence. *Tectonophysics* 662, 345–362. doi:10.1016/j.tecto.2015.05.006

Windley, B. F., and Xiao, W. J. (2018). Ridge subduction and slab windows in the Central Asian Orogenic Belt: tectonic implications for the evolution of an accretionary orogen. *Gondwana Res.* 61, 73–87. doi:10.1016/j.gr.2018.05.003

Wu, D. D., Li, S., Chew, D., Liu, T. Y., and Guo, D. H. (2021). Permian-Triassic magmatic evolution of granitoids from the southeastern Central Asian Orogenic Belt: implications for accretion leading to collision. *Sci. Chia (Earth Sci)* 64 (5), 788–806. (in Chinese with English abstract). doi:10.1007/s11430-020-9714-5

Wu, F. Y., Li, X. H., Yang, J. H., and Zheng, Y. F. (2007). Discussions on the petrogenesis of granites. *Acta Petrol. Sin.* 23 (6), 1217–1238. (in Chinese with English abstract).

Wu, F. Y., Sun, D. Y., Ge, W. C., Zhang, Y. B., Grant, M. L., Wilde, S. A., et al. (2011). Geochronology of the Phanerozoic granitoids in northeastern China. *J. Asian Earth Sci.* 41, 1–30. doi:10.1016/j.jseaes.2010.11.014

Xiao, W. J., Windley, B. F., Han, C. M., Liu, W., Wan, B., Zhang, J. E., et al. (2018). Late Paleozoic to early triassic multiple roll-back and oroclinal bending of the Mongolia collage in central Asia. *Earth-Sci Rev.* 186, 94–128. doi:10.1016/j.earscirev.2017.09.020

Xiao, W. J., Windley, B. F., Sun, S., Li, J. L., Huang, B. C., Han, C. M., et al. (2015). A tale of amalgamation of three Permo-Triassic collage systems in central Asia: Oroclines, sutures, and terminal accretion. *Annu. Rev. Earth. Pl. S. C.* 43, 477–507. doi:10.1146/annurev-earth-060614-105254

Xie, H., Wang, Y., Li, D., Zhou, G., and Zhang, Z. (2021). Late triassic magma mixing and fractional crystallization in the Qingchengzi Orefield, Eastern Liaoning Province: regional petrogenetic and metallogenic implications. *J. Earth Sci.* 32, 144–157. doi:10.1007/s12583-020-1114-3

Xing, K. (2022). *The magatic activity characteristies of Dashizhai Formation in Xi Ujimqin area, Inner Mongolia and its tectonic evolution significance. Master Dissertation. He Bei*. Shijiazhuang: Hebei GEO University, 1–53.

Xu, B., Wang, Z. W., Zhang, L. Y., Wang, Z. H., Yang, Z. N., and He, Y. (2018). The Xing-Mengintra continent orogenic belt. *Acta Petrol. Sin.* 34 (10), 2819–2844. (in Chinese with English abstract).

Xu, W. L., Pei, F. P., Wang, F., Meng, E., Ji, W. Q., Yang, D. B., et al. (2013). Spatial–temporal relationships of Mesozoic volcanic rocks in NE China: constraints on tectonic overprinting and transformations between multiple tectonic regimes. *J. Asian Ear Sci.* 74, 167–193. doi:10.1016/j.jseaes.2013.04.003

Yang, J. H., Wu, F. Y., Shao, J. A., Wilde, S., Xie, L., and Liu, X. (2006). Constraints on the timing of uplift of the Yanshan fold and thrust belt, north China. *Earth Planet Sci. Lett.* 246 (3-4), 336–352. doi:10.1016/j.epsl.2006.04.029

Zhang, J. H., Yang, J. H., Chen, J. Y., Wu, F. Y., and Wilde, S. A. (2018). Genesis of late Early Cretaceous high-silica rhyolites in eastern Zhejiang Province, southeast China: a crystal mush origin with mantle input. *Lithos* 296-299, 482–495. doi:10.1016/j.lithos.2017.11.026

Zhang, Q. Q., Zhang, S. H., Zhao, Y., and Hu, G. H. (2024). Compositionally variable basement and tectonic affinity of the Bainaimiao arc belt: implications for crustal growth of the Central Asian Orogenic Belt. *J. Asian Earth Sci.* 263, 106009. doi:10.1016/j.jseaes.2024.106009

Zhang, X. H., Wilde, S. A., Zhang, H. F., and Zhai, M. G. (2011). Early Permian high-K calc-alkaline volcanic rocks from NW Inner Mongolia, North China: geochemistry, origin and tectonic implications. *J. GeolSoc Lond.* 168 (2), 525–543. doi:10.1144/0016-76492010-094

Zhang, Y. J., Zhang, C., Ma, Y. F., Yang, T., Liu, Y., Du, J. Y., et al. (2022). Closure time of the eastern Paleo-Asian Ocean: constraint from permian-triassic strata and detrital zircon geochronology at southern great Xing'an mountains, inner Mongolia (China). *Acta Petrol. Sin.* 38 (9), 2781–2810. (in Chinese with English abstract). doi:10.18654/1000.0569/2022.09.16

Zhu, Y. F., Zhang, Y. D., Jiang, J. Y., and Lu, G. L. (2022). Study on ore-forming systems related with evolution of Paleo-Asian ocean in Xing-Meng Orogenic Belt. *Min. Deposita* 41 (3), 449–468. (in Chinese with English abstract). doi:10.16111/j.0258-7106.2022.03.001